Compact Low-Power Consumption Single-Mode Coupled Cavity Lasers

Shamsul Arafin, *Senior Member, IEEE*, Gordon B. Morrison, Milan L. Mashanovitch, *Senior Member, IEEE*,
Leif A. Johansson, *Member, IEEE*, and Larry A. Coldren, *Life Fellow, IEEE*

Abstract—Ultra-compact, widely-tunable and low-power InP-based four-section coupled-cavity lasers are designed and analyzed. Two Fabry–Pérot cavities of unequal lengths, each containing an amplifier and a phase-tuning section, are coupled together through low-loss Bragg grating. The theoretical analysis of such multisection lasers starts with calculating the poles of a linear transfer function of the entire resonator in order to obtain resonant wavelengths and wavelength-dependent threshold gains. The differential quantum efficiency and the power-current characteristics are then calculated to evaluate the laser performance. The effectiveness of the design procedure is verified by the experimental and proof-of-principle demonstration using simplified three-section lasers. Devices exhibit single-mode operation with a side-mode suppression ratio of over 24 dB and tuning range of 11.2 nm. These telecom-suitable lasers can be used as on-chip local oscillators in low-power integrated optical coherent receivers.

Index Terms—Coupled-cavity, Fabry-Pérot resonators photonic integrated circuits, integrated optoelectronics, tunable lasers.

I. INTRODUCTION

TUNABLE lasers and high-speed photodiodes in coherent photonic integrated circuit (PIC) receivers have always been of great interests for plenty of applications including optical communication [1], microwave photonics [2], sensing [2] and chip-scale frequency synthesis [4]. Given the tunable lasers consume most space and power in PIC receivers, a novel design for low-threshold, high-performance and short-cavity single-mode lasers with a wide tuning range is of utmost importance. Among several types of surface grating-based tunable lasers, sampled-grating distributed Bragg reflector (SG-DBR) [5], Y-branch [6], double-ring resonator [7], ring resonator mirror lasers [8] and grating-coupled sample reflector lasers [9] are some of the commonly used and commercially available ones. These devices, however, are relatively large and consume much

electrical power. Considering the class of widely tunable devices based on Vernier effect, for instance, the most compact in-line SG-DBR lasers are 1.5 mm long [10] and consume ∼0.4 W of power [11].

Compared to ring and coupler-based tunable lasers, in-line design is better because it can (i) provide minimal net cavity size by not having rings and couplers, (ii) give high axial fill factor since the device is free from non-tunable passive sections, and (iii) offer the widest mode spacing for a given gain length. Besides, lasers with the ring and passive couplers suffer from additional insertion loss and low mode-suppression ratio due to narrow mode spacing defined by the increased cavity length. Despite these obvious advantages obtained from in-line SG-DBR lasers, their sizes and power requirements are drawbacks for the development of compact and low-power photonic systems.

In the 1980s, a new and novel concept was proposed for simple and in-line lasers with single-mode emission, which are mainly based on coupling two Fabry-Pérot cavities [12]–[15]. Utilizing the same concept, the so-called coupled-cavity (C-C) lasers can be reconsidered to be one of the alternative ways in order to meet up the present and future size and power requirements. Recently, there have been a number of theoretical and experimental studies on C-C lasers reported by the scientific community [16], [17]. Some of the experimental studies report on the use of multimode interference reflector as a coupling element between two cavities [18]–[20]. With an epitaxial-regrowth-free cost-effective approach, devices made by this design had a footprint of 0.5 mm^2 and a power consumption of ∼0.2 W [18].

This work reports an active-passive integrated coupled-cavity design procedure where grating bursts as intercavity coupling elements are used. This study is more focused on the compactness, low-power consumption and wide tuning-range specifications of such devices. Compared to the state-off-the-art results on SG-DBR lasers reported in [10], [11] our proposed C-C laser is 5 times smaller in size, and it consumes 7 times less electrical power for its full operation with the optical output power of 5 mW. Due to potentially short cavities, high fill-factors for the gain regions, and compatibility with simple PIC fabrication processes, the C-C design is more efficient, compared to matured- and low-risk SG-DBR lasers. Therefore, these devices are well-suited for developing next-generation compact, low-power and efficient photonic systems.

This paper is organized as follows: This paper begins with a discussion of the C-C laser design which describes the

S. Arafin and L. A. Coldren are with the Department of Electrical and Computer Engineering, University of California, Santa Barbara, CA 93106 USA (e-mail: sarafin@ece.ucsb.edu; coldren@ece.ucsb.edu).

G. B. Morrison, M. L. Mashanovitch, and L. A. Johansson are with the Freedom Photonics LLC, Santa Barbara, CA 93117 USA (e-mail: gordon@freedomphotonics.com; mashan@freedomphotonics.com; leif@freedomphotonics.com).
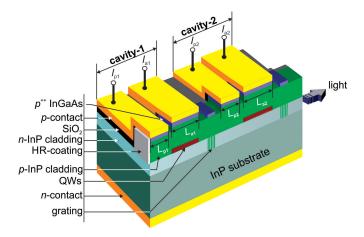
Fig. 1. Schematic cross-sectional view of a C-C laser with four electrodes. L_{p1} and L_{a1} are the passive and active sections lengths of cavity-1, whereas L_{p2} and L_{a2} passive and active sections lengths of cavity-2. The currents I_a and I_p are injected in the active and passive sections of FP cavities, respectively.
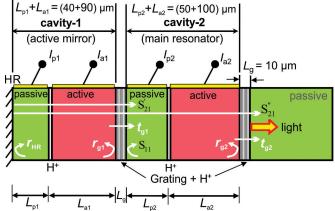

Fig. 2. Simplified schematic illustration of a coupled-cavity laser. The rightmost-long section labelled by "Passive" is not the part of the resonator.

calculation of scattering matrices and how it leads us to find the threshold gains and wavelengths of the modes of the entire coupled system. This section also provides results obtained from the simulation of the differential quantum efficiency, yielding power-current characteristics, and wavelength tuning behavior of the laser. This is then followed by a discussion of the performance improvement concept, power budget estimation and tuning range extension of the device. We then present the processing details of the simplified C-C laser. Finally, the performance characterization of initial experimental devices is reported.

II. COUPLED-CAVITY LASER DESIGN

Fig. 1 shows a schematic cross-sectional view of a four-section C-C laser which is comprised of two cavities, denoted as cavity-1 and cavity-2. They are in-line coupled via first-order surface grating bursts. Each cavity includes active and passive regions that are electrically isolated by proton implants. Cavity-1 can be referred to as an "active mirror", while cavity-2 as a "main resonator", providing most of the gain. The mode selected by the C-C lasers is nothing but a longitudinal FP mode that has the lowest cavity loss determined by the Vernier effect, resulting from unequal cavity lengths of these two FP cavities. Since the basic operating principle and the mechanism of the mode selectivity in such lasers are well-described in a number of literatures [12], [14] we will immediately move into the theoretical analysis of our proposed compact and low-power single-mode C-C lasers with a unique configuration.

A. Calculation of Scattering Matrices

A theoretical analysis of the C-C lasers requires simultaneous consideration of the gain and loss in the two FP cavities after taking the reflection and transmission at the intercavity coupling interface into account. Scattering matrices were used to perform the numerical analysis of such complex laser structures. The primary objective is to find the resonant longitudinal modes of the coupled system by calculating the corresponding emission wavelengths and their respective gains required to reach thresh-

old. Fig. 2 illustrates a simplified schematic of a representative C-C laser which helps to perform the numerical analysis. In this example, cavity-1 is formed by independent and electrically-isolated 90-μm-long active and 40-μm-long passive sections. The gain of the active section and the phase of the passive section can be independently controlled by currents, denoted by I_a and I_p, respectively. Similarly, cavity-2 consists of independent 100-μm-long active and 50-μm-long passive sections, whose lengths are represented by L_{a2} and L_{p2}. The mode spacings for cavity-1 and cavity-2 are calculated to be 2.4 nm and 2.1 nm, respectively, resulting a spacing mismatch of 0.3 nm and a possible repeat mode every 16.8 nm. The phase tuning sections enable the modes to be tuned continuously.

Prior to obtaining the resonant longitudinal modes of the entire coupled system, it is important to understand how cavity-1 serves as an active mirror modulating the loss of the FP modes via an equivalent mirror. The gain-providing mirror (i.e. cavity-1) can be represented by an effective mirror with complex reflectivity S_{11} which can be written in the form [21]

$$S_{11} = -r_{g1} + \frac{r_{HR} t_{g1}^2 e^{-2j\tilde{\beta}L_1}}{1 - r_{HR} r_{g1} e^{-2j\tilde{\beta}L_1}} \qquad (1)$$

where r_{g1} and r_{HR} are amplitude reflection coefficients of the grating and the high-reflection mirror coating, respectively, t_{g1} transmission coefficient across the grating interface at cavity-1, $\tilde{\beta}$ complex propagation constant and L_1 the total length of active and passive sections in cavity-1. $\tilde{\beta}$ is defined as

$$\tilde{\beta} = \beta + j\beta_i$$
$$= \frac{2\pi\bar{n}}{\lambda} + j\left(\frac{g}{2} - \frac{\alpha_i}{2}\right) \qquad (2)$$

where β is the average propagation constant, $\bar{n}$ the effective refractive index of the mode, g the modal gain and α_i the internal modal loss.

The net reflection coefficient from the grating can be defined by the following approximate sinc-function spectral response:

$$r_{g1} \approx \kappa L_g * \text{sinc}\left(\frac{2\pi L_g \bar{n}}{\lambda} - \frac{2\pi L_g \bar{n}}{1.55}\right) \qquad (3)$$
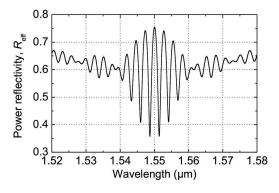
Fig. 3. The effective mirror reflectivity for cavity-2 due to cavity-1, when current applied to cavity-1 and its phase tuning section is 1 mA.
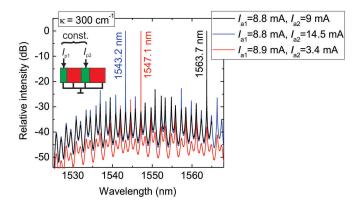

Fig. 4. Example plots of $S''_{21}(\lambda)$ to obtain "thresholds" for three mode solutions where the phase currents in both cavities are constant.

where L_g is the grating length, κ the reflection per unit length. The grating reflection is relatively weak with $\kappa = 300 \text{ cm}^{-1}$ and $L_g = 10 \, \mu$m, but a tuning range of $\sim$30 nm is still possible. The net reflection peak is assumed to be at Bragg wavelength, i.e. 1.55 μm. Note that the reference planes for the gratings are placed at an index down step on their left side in Fig. 2, and they have an integer number of periods. Thus, the reference planes on their right sides are displaced by a half-grating period from the last index down step on that side. Although arbitrary, this selection results in the correct phasing of the two terms in S_{11} shown in (1).

The transmission magnitude through the grating mirror becomes

$$t_{g1} = \sqrt{\left(1 - r_{g1}^2\right) e^{-\alpha_g * L_g}} \qquad (4)$$

And its transmission phase is given by its length. For simplicity, the gain function is often approximated by a simple Lorentzian lineshape with a peak at 1550 nm [21],

$$L(\lambda) = \left(\frac{7 \times 10^{-3}}{4(\lambda - 1.55)^2 + 7 \times 10^{-3}} \right) \qquad (5)$$

Experimental material gain g with a number of quantum wells N_{QW} as a function of injected current density J for 1.55 μm lasers is well represented by the g-J relationship

$$g = 583 \times \ln\left(\frac{\eta_i J}{N_{\text{QW}} 81} \right) \text{cm}^{-1} \qquad (6)$$

where η_i the current injection efficiency which can be assumed to be 0.8 for initial simulations [21].

Finally, using (2)–(6) in (1) and by applying 1 mA current in both active and passive section of cavity-1, the modulated effective mirror reflectivity $|r_{\text{eff}}|^2$, i.e., what cavity-2 sees due to cavity-1 is plotted as a function of λ in Fig. 3.

Given this basic understanding, we now move on to obtain the threshold gain and resonant wavelengths of the lasing modes. This can be done by finding the net transfer function $S''_{21}(\lambda)$ of the entire system. The poles of this transmission spectrum indicate the resonant wavelengths of the laser for the particular sets of modal gain values $(\Gamma g_{\text{th}-1}, \Gamma g_{\text{th}-2})$, required to develop a strong maximum of $|S''_{21}(\lambda)|$ as the gain is increased through electrical pumping. Note that Γ, the transverse-lateral confinement factor, is assumed to be 0.1 in the analysis. This

technique is used to determine the pairs of threshold gains of the two active sections for the possible lasing modes.

In order to obtain $S''_{21}(\lambda)$, we need to find the transmission spectrum $S'_{21}(\lambda)$ through first grating in cavity-1.

$$S'_{21}(\lambda) = \frac{t_{\text{HR}} t_{g1} e^{-j\tilde{\beta}L_1}}{1 - r_{\text{HR}} r_{g1} e^{-2j\tilde{\beta}L_1}} \qquad (7)$$

Finally, the net transfer function across the entire device from the HR mirror to the right-most grating

$$S''_{21}(\lambda) = \frac{S'_{21} t_{g2} e^{-j\tilde{\beta}L_2}}{1 - r_{g2} S_{11} e^{-2j\tilde{\beta}L_2}} \qquad (8)$$

where r_{g2} is the reflection coefficient of the output grating mirror and L_2 the total length of active and passive sections in cavity-2.

Using (1)–(7) in (8), we get a fairly complex equation. By solving it, the poles of $S''_{21}(\lambda)$ for the mode solutions are obtained, as shown in Fig. 4 for three example cases. The currents in active sections of cavity-1 and cavity-2 are varied, while the currents in phase sections of both cavities are kept constant, to obtain these solutions. As can be seen, a small change in I_{a1} may require a significantly different value of I_{a2}, and this causes a relevant change in the lasing mode wavelength. Dithering the phase currents will help to optimize the modal selectivity even better than the plots in Fig. 4.

Fig. 5(a) gives threshold modal gain pair solutions for wavelengths ranging from 1532 nm to 1568 nm for the device presented in Fig. 2. A 2D plot of the threshold modal gain of cavity-1, $\Gamma g_{\text{th}-1}$, versus the threshold modal gain of cavity-2, $\Gamma g_{\text{th}-2}$ is shown here. The corresponding current and current densities required in each gain section to reach threshold with a fixed phase current in both passive sections is also shown here. The data is obtained by fixing $\Gamma g_{\text{th}-1}$ and solving for $\Gamma g_{\text{th}2}$ and λ for each given $\Gamma g_{\text{th}-1}$ over a prescribed range of wavelengths. $\Gamma g_{\text{th}-1}$ is then increased and the process is repeated. The mode wavelengths and the corresponding threshold gains shown in the upper right corner of Fig. 5(a) are not desirable from a practical point of view, since those wavelengths can be obtained with lower threshold currents, if currents in the two passive sections are tweaked properly.
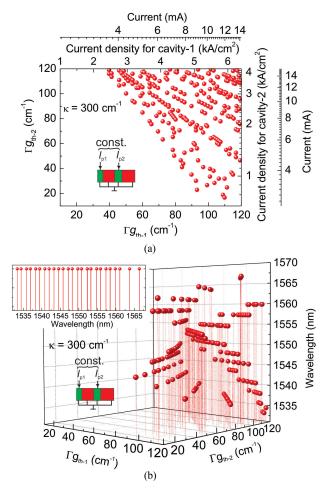
Fig. 5. (a) 2D plot for modal threshold gain, Γg_{th-1} vs Γg_{th-2} and corresponding current densities for the lasing modes, where $\kappa = 300$ cm^{-1} and constant phase current = 1 mA, and (b) the corresponding 3D trajectories, showing modal threshold gain, Γg_{th-1} vs Γg_{th-2} and corresponding resonant wavelengths as a third dimension.

Since Fig. 5(a) does not provide information about resonant wavelengths, it is convenient to plot 3D trajectories as shown in Fig. 5(b), where wavelength is included as a third dimension. The inset of Fig. 5(b) illustrates the wavelengths that cover the entire range between 1532 nm and 1568 nm for the realistic condition, $\Gamma g_{th} \leq 120$ cm^{-1}.

B. Calculation of Differential Quantum Efficiency

With the threshold modal gain pair solutions for wavelengths ranging from 1532 nm to 1568 nm calculated, we can now determine the differential quantum efficiency η_d of the C-C laser. In such a way, the output characteristics of this complex resonator can also be determined. The differential efficiency can be simply defined as the cavity output modal loss relative to the total modal loss (which is the threshold modal gain), reduced by the injection efficiency. For simplicity, we assume that there is no excess scattering loss caused by the rightmost grating mirror or the leftmost high-reflection coated mirror, so that all output cavity loss is coupled into the output waveguides. Hence, for each wavelength and modal gain pair, η_d is given to a good
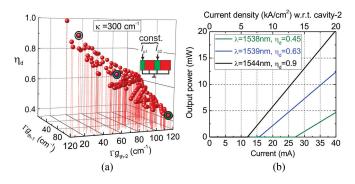

Fig. 6. Output characteristics of C-C lasers, (a) 3D trajectories, showing modal threshold gain, Γg_{th-1} vs Γg_{th-2} and corresponding differential quantum efficiency as a third dimension, and (b) power-current characteristics as a function of differential quantum efficiency. (w.r.t. = with respect to)

approximation by [21, Appendix 5]:

$$\eta_d = \eta_i \frac{\frac{1}{L} \ln \left(\frac{1}{r_{g2} \times r_{HR}} \right)}{\frac{L_{a1}}{L} \Gamma g_{th,1} + \frac{L_{a2}}{L} \Gamma g_{th,2}} \qquad (9)$$

where L is the total cavity length including the phase tuning sections and the gratings. For our η_d calculations, η_i and r_{HR} are approximated as 0.8 and 1, respectively. Note that the denominator of (9) is the net cavity modal gain, i.e., the sum of the net modal gains of each cavity, including the axial confinement factors. This could have been more simply written as $[< g_{th,1} > + < g_{th,2} >]$, where the $< >$ denote a 3D averaging of the gain material in each cavity over the entire mode.

Fig. 6(a) displays the threshold modal gain pair solutions for differential efficiencies ranging from 0.45 to 0.9, by applying a fixed phase current in both passive sections of the device. These values represent wavelength solutions across the entire 36 nm tuning range of the laser using a coupling coefficient, $\kappa = 300$ cm^{-1}. Given the injection currents applied to each cavity in order to reach threshold, the corresponding resonant wavelengths and the differential efficiency are known, the output optical power-current (*P-I*) characteristics can be calculated from (9) to obtain the following expression,

$$P = \eta_d \frac{hc}{\lambda q} \left(I - (I_{th,1} + I_{th,2}) \right) \qquad (10)$$

where *h, c, q* are constants; and λ, I_{th-1}, I_{th-2} are the values obtained from the solution, representing the resonant emission wavelength, and threshold currents for the cavities, respectively. Finally, *P-I* curves are plotted for three different solutions, differentiated by their resonant wavelength and differential efficiency, as shown in Fig. 6(b). Equations (9) and (10) require that there be some gain in both cavities so that power levels are not drastically different [21, Appendix 5].

C. Quasi-Continuous Tuning

The resonant wavelengths, covering the entire range between 1532 nm and 1568 nm for the realistic condition, $\Gamma g_{th} \leq 120$ cm^{-1} is shown in the inset of Fig. 5(b). It is of great importance to check whether missing wavelength values between adjacent cavity modes in Fig. 7 can be filled out
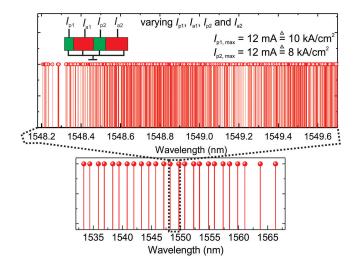
Fig. 7. The lasing modes covering the emission wavelength range between 1532 nm and 1568 nm by fixing the phase currents (bottom). Continuous tuning is possible between any two adjacent cavity-modes by varying the phase currents in both cavities (top).

electronically. To save computation space and time, only the region around 1550 nm, occupying two cavity modes, is simulated. It is found that any wavelength can be obtained by changing the phase current independently in phase sections of cavity-1 and cavity-2, as shown in Fig. 7. However, because of the mode-hoping behavior, the device is expected to exhibit quasi-continuous tuning.

D. Devices With Higher κ

The above theoretical results use a grating with $\kappa = 300\,\mathrm{cm}^{-1}$, which is the value utilized in standard and large-area SGDBR lasers [5]. In spite of showing great potential of C-C lasers, evidenced by the simulated results shown so far, the gratings used have very low-reflectivity mirrors, requiring relatively high threshold current densities for the device, sometimes $>10\,\mathrm{kA/cm^2}$. Such unrealistic current densities may prevent such devices even from lasing. Thus, it is of significant interest to consider higher coupling coefficient grating mirrors [22], in order to increase the reflectivity of 10-μm-long grating mirrors and reduce the threshold currents and power dissipations.

In order to confirm such improvements, numerical calculations were performed for the same resonator structure with a higher $\kappa = 600\,\mathrm{cm}^{-1}$ and $900\,\mathrm{cm}^{-1}$. As can be seen in Fig. 8(a), the mode solutions have lower modal gain values, indicating that less current is required to reach threshold compared to the structure with $\kappa = 300\,\mathrm{cm}^{-1}$. The threshold current in a resonators especially with $\kappa = 900\,\mathrm{cm}^{-1}$ is drastically reduced, even as low as $\sim 6\,\mathrm{mA}$ for $\eta_d = 0.61$. At the same time, the entire wavelength range between 1532 nm and 1568 nm is covered by these solutions with a more realistic condition, $\Gamma g_{\mathrm{th}} \leq 120\,\mathrm{cm}^{-1}$.

The improved performance is further confirmed through the *P-I* characteristics with different κ for a pair of η_d values, calculated by the threshold modal gain pair solutions. Note that for $\kappa = 900\,\mathrm{cm}^{-1}$, the optical output power as high as 5 mW at
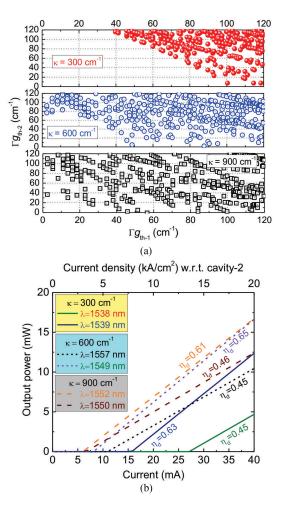

Fig. 8. (a) 2D plot for modal threshold gain, $\Gamma g_{\mathrm{th}-1}$ vs $\Gamma g_{\mathrm{th}-2}$ for lasers with different coupling coefficients. Lasers with the coupling coefficient as high as 900 cm^{-1} obviously require less modal gain to reach threshold, and (b) calculated power-current *(P-I)* characteristics as a function of differential quantum efficiency for grating mirrors of different κ for a grating length of 10 μm.

TABLE I
POWER CONSUMPTION ESTIMATE OF THE C-C LASERS
WITH $\kappa = 900\,\mathrm{cm}^{-1}$ FOR 5 mW OUTPUT POWER

Section	Number	Current (mA)	Voltage (V)	Power (mW)
Gain	2	(6 + 10) = 16	1.2, 1.4	21.2
PT	2	(12 + 12) = 24	1.4	33.6
Total		40		$\sim$**55**

PT = phase tuner.

$\eta_d = 0.61$ can be achieved for the total injection current of only 15 mA in two active sections (see Fig. 8(b)).

E. Power Budget Estimation

Table I presents the total maximum power consumption of the fully-operational C-C laser with $\kappa = 900\,\mathrm{cm}^{-1}$ and optical output power of 5 mW. There are two phase tuning sections integrated in the chip. It should be noted that it is possible to achieve full wavelength tuning using these two phase sections of the laser.
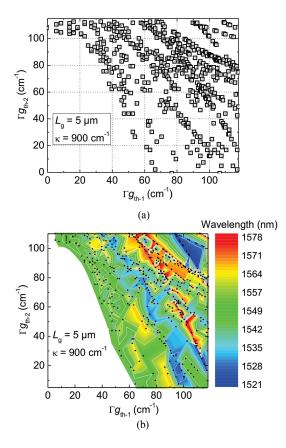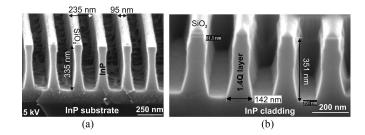
Fig. 10. (a) Holographically patterned deep-grating etched by methane/hydrogen/argon-RIE for (a) InP, and (b) quaternary waveguide layers.

obtained experimentally for a grating of length 10 μm.

$$r_g = \tanh\left(\kappa L_g\right) \tag{11}$$

Thus, $\kappa = 880$ cm^{-1}. Utilizing deeply-etched grating with $\kappa = 880$ cm^{-1} and (11), power reflectivity can be calculated to be 0.5.

For shallow-etch depths, the corrugated grating can be seen as a small perturbation, giving a negligible scattering loss. The loss increases with increased etch depth and importantly, the maximum loss occurs at an etch depth of about half the waveguide thickness. As the etch depth is increased further, the loss starts to roll off. As the grating etch depth penetrates across the entire slab waveguide thickness, a symmetric perturbation is created, thus reducing the scattering loss [23].

H. Deep Grating Fabrication

There have been experimental efforts in fabricating such high-κ mirrors. Several etching recipes for such deep gratings with high aspect ratio and straight sidewalls were used. While methane-based reactive ion etch (RIE) is a common etching method for InP-based embedded square gratings, the polymer buildup and the photoresist erosion problems generally limit the depth of square gratings beyond 100 nm. However, using our optimized recipe, the grating pattern was successfully transferred to InP and 1.4-quaternary (Q) waveguide layers by methane/hydrogen/argon (MHA) RIE method. Fig. 10(a) and (b) shows examples of the fabricated gratings of InP and 1.4Q layers, respectively, with SiO$_2$ as the etch mask. A nearly square grating profile of ~350 nm depth, being suitable for the C-C lasers, is produced using an optimized etched recipe. Moreover, the groove opening, clean bottoms and profile straightness are found to be acceptable for $\kappa = 900$ cm^{-1}. A layer of 50 nm SiO$_2$ was deposited on the sample by a plasma enhanced chemical vapor deposition (PECVD) method as the hard mask. Photoresist was then spun on top of this SiO$_2$ layer. The interference grating patterns are generated by the holographic exposure on the photoresist and are transferred to SiO$_2$ by a CF$_4$/CHF$_3$/O$_2$ RIE. Finally, semiconductor layers were etched to realize the deep grating.

III. COUPLED-CAVITY LASER FABRICATION

For the sake of simplicity and proof-of-principle demonstration, devices were processed with one phase section and two gain sections. Cavity-1 is formed by 90-μm and 40-μm long gain

Fig. 9. (a) $\Gamma g_{\text{th}-1}$ vs $\Gamma g_{\text{th}-2}$ for lasers with a grating length of 5 μm and $\kappa = 900$ cm^{-1}, and (b) contour plot of the emission wavelength as a function of the modal gain. The emission wavelength range between 1521 nm and 1578 nm can be covered by the cavity modes where the phase current is fixed in each cavity.

F. Devices With Shorter Grating

Despite this reasonably good performance of C-C lasers with coupling coefficient $\kappa = 900$ cm^{-1}, further improvement is still required for the device with wide tuning range as high as 50 nm in order to cover the whole-C band. This is because the grating with a length of 10 μm unfortunately cannot provide such desired wide tuning range. It should be noted that all the simulation results of C-C lasers presented so far used $L_g = 10\,\mu$m. This clearly necessitates of doing the analysis of the device with a grating length as short as 5 μm.

Fig. 9 (a) displays the threshold modal gain pair solutions for $L_g = 5\,\mu$m, by applying a fixed phase current in both passive sections of the structure. Most importantly, this should be technologically achievable with only slight increase in cavity loss in the device. This is reflected by the mode solutions at a bit higher ($\Gamma g_{\text{th}-1}$, $\Gamma g_{\text{th}-2}$) values compared to the case $L_g = 10\,\mu$m. These values represent wavelength solutions across the entire >50 nm tuning range of the laser using a coupling coefficient, $\kappa = 900$ cm^{-1}, as presented by the contour plot in Fig. 9(b).

G. Deep Grating

One possible way of increasing the coupling coefficient of such grating mirrors is to use deeply-etched grating, as demonstrated by Chen et al. [22], where 50% power reflectivity was
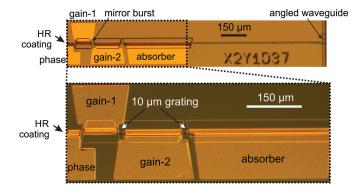
Fig. 11. Microscope image of a fully-processed processed C-C laser followed by an absorber.

and passive sections, respectively, whereas cavity-2 consists of only 100-μm-long active sections. The device is followed by a long absorber section that allows the accurate on-chip static characterization decoupled from facet coupling loss. The absorber may also be forward biased to operate as an integrated booster amplifier. The offset quantum well (OQW) integration platform [24] was chosen for processing C-C lasers. The OQW integration platform has quantum wells offset from the center of the waveguide, with a confinement factor of 10%. The definition of active and passive areas required a wet etch of the top 200-nm-thick InP layer and quantum wells which were selectively removed by the etch-stop layer. This makes the OQW integration platform the simplest way to combine active and passive components on chip. First-order grating mirrors were defined on the device using electron beam lithography. Devices utilized standard shallow grating ($\kappa \sim 300$ cm^{-1}) by etching down to 80 nm in the 1.4Q layer. After grating definition, a blanket p-cladding and p^+-contact layer were regrown. Surface ridge waveguide with a width of 2–3.3 μm was then formed. After that, p-contact vias were opened to allow metallization of p-contact layer. P-side contact metal layers were deposited to allow p-side electrical connection. We implanted the regions between p-side contacts on the PIC to provide electrical isolation. The wafer backside was then thinned down to 140 μm and metallized. After cleaving and anti-reflection (AR) coating of the waveguide facets, devices were singulated, and mounted to a ceramic carrier in order to provide heat-sink and electrical connection for contacting the device. After wirebonding, devices were tested. In the device, the light outcoupling port was accessed by an angled cleaved facet with AR coating to suppress back-reflection. A microscope picture of the fully-processed PIC with a C-C laser followed by an absorber is shown in Fig. 11.

IV. DEVICE CHARACTERIZATION

Temperature dependent continuous-wave (CW) P-I-V characteristics of devices were measured on a Peltier-cooled copper heatsink, as shown in Fig. 12. The device shows CW operation up to room-temperature. Measurements were performed when the current in cavity-1 is fixed to 17 mA and no current in the phase section is applied. On-chip absorber, reverse biased by
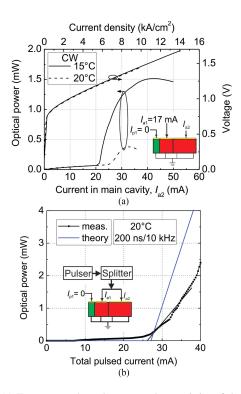

Fig. 12. (a) Temperature dependent P-I-V characteristics of the C-C laser. Schematic of the device biasing is shown as inset, and (b) pulsed P-I characteristics of the same device, which is superimposed on the plot obtained from the theory.

2 V, was used as a photodetector with an assumed responsivity of 1 A/W to measure the optical power coming out from the device. The maximum off-chip CW output power from the laser to a lensed fiber is 0.4 mW at 15 °C and when the absorber was forward biased to operate as a booster amplifier. In spite of the reasonable series resistance in the device and good diode turn-on voltage, verified by I-V characteristics and good material quality of the sample, devices exhibit higher threshold current density compared to the value obtained through numerical simulation. This could be most probably due to grating with $\kappa < 300$ cm^{-1} which introduces high scattering loss. Such a loss was not taken into account in the theoretical analysis.

In order to minimize joule heating effect, pulsed measurement was performed using a pulser with a low duty cycle (e.g. 0.2%). A resistive 50:50 power splitter was used after the pulser to split the pulse current into two paths in order to drive two gain sections of the device. Since the current splitting depends upon the load in these two paths, current probes were connected in each path to know the current going into each gain section. The pulsed and the theoretical P-I characteristics, as shown in Fig. 12(b), are superimposed on each other. Device exhibits lasing when the gain-1,2 sections are pumped by 11.9 mA, 14.7 mA, respectively. This operation with modal gain $\Gamma g_{\text{th}-1}$, $\Gamma g_{\text{th}-2}$ can be described by a point (109 cm^{-1}, 115 cm^{-1}) in Fig. 5(a), if one assumes a $\kappa = 300$ cm^{-1}. The threshold currents are in the expected range for the resulting low mirror reflectivities, corresponding to Figs. 6(b) and 8(b) [with solid lines], and the lower differential efficiencies are explained by experimental
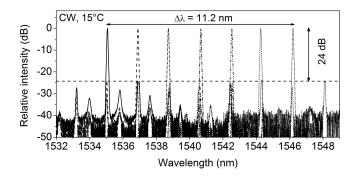
Fig. 13. Spectra of C-C lasers by varying current in cavity-1 and cavity-2, while the phase section current is kept constant.
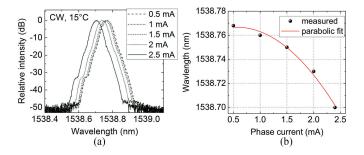

Fig. 14. (a) Fine tuning of the emission wavelength by changing current in the phase section, while the currents in gain sections are constant, and (b) wavelength tuning curve as a function of phase current.

injection efficiencies that are considerably less than unity, which was assumed in the theoretical plots.

The emission spectra of the C-C device are shown in Fig. 13, which was obtained by varying the current in cavity-1 and cavity-2 and keeping the current in the phase section constant. The wavelength tuning range of such devices is measured to be 11.2 nm, whereas the designed repeat mode-spacing of the laser was 16.8 nm. This could be attributed to the low-κ mirrors due to under etched mirrors, resulting in high-threshold devices. This results in device self-heating, which causes early thermal rollover in the device. As can be seen in Fig. 13, the device exhibits single-mode operation with a side-mode suppression ratio (SMSR) of over 24 dB over the entire operating range.

The fine tuning of the emission wavelength was measured by varying the phase-section current at a constant current in both cavities. Fig. 14(a) shows the change of the emission wavelength as a function of phase section, yielding mode-hop-free tuning range around 0.07 nm. However, a mode hop occurs if the phase section is tuned beyond the axial mode spacing within the laser of approximately 1.1 nm, if the other currents are not simultaneously adjusted. The wavelength tuning curve of the phase tuning section follows a square root behavior with respect to injected current, indicating primarily radiative recombination in this region, as can be seen in Fig. 14(b).

V. CONCLUSION

A comprehensive theoretical analysis of small-size and low-power consumption linear coupled-cavity lasers is proposed in this study. A description of step-by-step design procedures to realize such photonic-integrated circuit compatible devices

is also provided here, serving as guidelines for the laser designers to model next-generation single-mode, and widely tunable devices. We have then experimentally demonstrated active-passive integrated C-C lasers with a simple configuration and compared the device results with the theory. The tuning range of these single-mode devices is measured to be 11.2 nm, less than the designed value, but partially explained by relatively low-reflectivity mirrors that require quite high gains and current densities. The relevant works for developing high-performance C-C lasers with short-deep grating to obtain wide tuning ranges as high as 50 nm are in progress and will be presented in future reports. Owing to their advantages of compact size, low-power, simple fabrication technique and full-integrability with standard processes into advanced PIC designs, these lasers should be useful for many diverse applications.

REFERENCES

[1] V. Houtsma *et al.*, "Manufacturable monolithically integrated InP dual-port coherent receiver for 100G PDM-QPSK applications," in *Proc. Opt. Fiber Commun.*, Los Angeles, CA, 2011, pp. 1–3.

[2] A. Ramaswamy *et al.*, "Integrated coherent receivers for high-linearity microwave photonic links," *J. Lightw. Technol.*, vol. 26, no. 1, pp. 209–216, Jan. 2008.

[3] M. D. Turner, S. Datta, G. W. Kamerman, D. Becker, A. Joshi, and R. Howard, "Ultra-fast coherent optical system for active remote sensing applications," *Proc. SPIE, Laser Radar Technol. Appl. XIII*, vol. 6950, 2008, Art. no. 695008.

[4] S. Arafin *et al.*, "Towards chip-scale optical frequency synthesis based on optical heterodyne phase-locked loop," *Opt. Express*, vol. 25, no. 2, pp. 681–695, 2017.

[5] V. Jayaraman, Z.-M. Chuang, and L. A. Coldren, "Theory, design, and performance of extended tuning range semiconductor lasers with sampled gratings," *IEEE J. Quantum Electron.*, vol. 29, no. 6, pp. 1824–1834, Jun. 2002.

[6] J.-O. Wesstrom, G. Sarlet, S. Hammerfeldt, L. Lundqvist, P. Szabo, and P.-J. Rigole, "State-of-the-art performance of widely tunable modulated grating Y-branch lasers," in *Proc. Opt. Fiber Commun.*, Los Angeles, CA, 2004, p. 389.

[7] S. Matsuo and T. Segawa, "Microring-resonator-based widely tunable lasers," *IEEE J. Sel. Top. Quantum Electron.*, vol. 15, no. 3, pp. 545–554, May/Jun. 2009.

[8] S. Srinivasan, M. Davenport, T. Komljenovic, J. Hulme, D. T. Spencer, and J. E. Bowers, "Coupled-ring-resonator-mirror-based heterogeneous III-V silicon tunable laser," *IEEE Photon. J.*, vol. 7, no. 3, 2015, Art. no. 2700908.

[9] P.-J. Rigole *et al.*, "114-nm Wavelength tuning range of a vertical grating assisted codirectional coupler laser with a super structure grating distributed Bragg reflector," *IEEE Photon. Technol. Lett.*, vol. 7, no. 7, pp. 697–699, Jul. 1995.

[10] M. Lu *et al.*, "Monolithic integration of a high-speed widely tunable optical coherent receiver," *IEEE Photon. Technol. Lett.*, vol. 25, no. 11, pp. 1077–1080, Jun. 2013.

[11] M. Lu, "Integrated optical phase-locked loops," Ph.D. dissertation, Dept. Electr. Comput. Eng., Univ. California, Santa Barbara, CA, USA, 2013.

[12] L. A. Coldren and T. L. Koch, "Analysis and design of coupled-cavity lasers-Part I: threshold gain analysis and design guidelines," *IEEE J. Quantum Electron.*, vol. QE-20, no. 6, pp. 659–670, Jun. 1984.

[13] L. B. Allen, H. G. Koenig, and R. R. Rice, "Single frequency injection laser diodes for integrated optics and fiber optics applications," in *Proc. Soc. Photon. Opt. Eng.*, San Diego, CA, 1978, pp. 110–117.

[14] C. H. Henry and R. F. Kazarinov, "Stabilization of single frequency operation of coupled-cavity lasers," *IEEE J. Quantum Electron.*, vol. QE-20, no. 7, pp. 733–744, Jul. 1984.

[15] R. J. Lang and A. Yariv, "An exact formulation of coupled-mode theory for coupled-cavity lasers," *IEEE J. Quantum Electron.*, vol. 24, no. 1, pp. 66–72, Jan. 1988.

[16] D. Lenstra, "Self-consistent rate-equation theory of coupling in mutually injected semiconductor lasers," *Proc. SPIE, Phys. Simul. Optoelectron. Devices XXV*, vol. 10098 , 2017, Art. no. 100980K.

[17] P. Bardella, W. Chow, and I. Montrosset, "Design and analysis of enhanced modulation response in integrated coupled cavities DBR lasers using photon-photon resonance," *Photonics*, vol. 3, no. 1, 2016, Art. no. 4.

[18] D. D'Agostino, D. Lenstra, H. P. Ambrosius, and M. K. Smit, "Coupled cavity laser based on anti-resonant imaging via multimode interference," *Opt. Lett.*, vol. 40, no. 4, pp. 653–656, 2015.

[19] W. Yao, G. Gilardi, D. D'Agostino, M. K. Smit, and M. J. Wale, "Monolithic tunable coupled-cavity WDM transmitter in a generic foundry platform," *IEEE Photon. Technol. Lett.*, vol. 29, no. 6, pp. 496–499, Mar. 2017.

[20] P. E. Morrissey, N. Kelly, M. Dernaika, L. Caro, H. Yang, and F. H. Peters, "Coupled cavity single-mode laser based on regrowth-free integrated MMI reflectors," *IEEE Photon. Technol. Lett.*, vol. 28, no. 12, pp. 1313–1316, Jun. 2016.

[21] L. A. Coldren, S. W. Corzine, and M. L. Mashanovitch, *Diode Lasers and Photonic Integrated Circuits*, 2nd ed. Hoboken, NJ, USA: Wiley, 2012.

[22] C.-H. Chen, J. Klamkin, L. A. Johansson, and L. A. Coldren, "Design and Implementation of ultra-compact grating-based 2×2 beam splitter for miniature photonic integrated circuits," in *Proc. Opt. Fiber Commun.*, Los Angeles, CA, 2008, pp. 1–3.

[23] C.-H. Chen, J. Klamkin, S. C. Nicholes, L. A. Johansson, J. E. Bowers, and L. A. Coldren, "Compact beam splitters with deep gratings for miniature photonic integrated circuits: design and implementation aspects," *Appl. Opt.*, vol. 48, no. 25, pp. F68–F75, 2009.

[24] J. W. Raring *et al.*, "Advanced integration schemes for high-functionality/high-performance photonic integrated circuits," *Proc. SPIE, Photon. Packag. Integr. VI*, vol. 6126, 2006, Art. no. 61260H.

Shamsul Arafin (S'08–M'12–SM'17) received the B.Sc. degree in electrical and electronics engineering from the Bangladesh University of Engineering and Technology, Dhaka, Bangladesh, in 2005, the M.Sc. degree in communication technology from Universität Ulm, Ulm, Germany, in 2008, and the Ph.D. degree from the Technische Universität München, Walter Schottky Institut, Munich, Germany, in 2012. He is currently working as an Assistant Project Scientist with the University of California Santa Barbara (UCSB), Santa Barbara, CA, USA. Prior to joining UCSB, he worked as a Postdoctoral Research Scholar in the Device Research Laboratory, University of California at Los Angeles, CA. Till now, he has authored and coauthored more than 70 papers in leading technical journals and international conferences.

Gordon B. Morrison received the B.A.Sc. degree (Hons.) from the Simon Fraser University, Vancouver, BC, Canada, in 1997, and the Ph.D. degree from McMaster University, Hamilton, ON, Canada, in 2002, both in engineering physics. His doctoral work, under Prof. D. T. Cassidy, focused on modeling and characterization of gain-coupled DFB lasers. From 1998 to 2002, he spent more than a year at Nortel Networks, ON, Canada, as a Graduate Student Researcher. From 2002 to 2003, he was a Post-Doctoral Fellow with McMaster University, where he was involved in development of a model for asymmetric-multiple-quantum-well gain and worked on process development for quantum-well intermixing. In June 2003, he joined the Department of Electrical and Computer Engineering, University of California, Santa Barbara, as a Visiting Assistant Research Engineer in Prof. L. Coldren's group, where he participated in the design, fabrication, and characterization of small footprint DBR EMLs using quantum-well-intermixing technology, and used photocurrent spectroscopy to characterize and optimize photonic integrated circuits. In 2005, he joined ASIP (formally III-V Photonics), Houten, The Netherlands, and in 2006 joined Apogee Photonics (formerly ASIP/T-Networks), Allentown, PA, where he worked on uncooled 1310 EML technology, 40G EA modulators, and monolithically integrated SOA/EA products. Apogee photonics was acquired by CyOptics Inc, Breinigsville PA, and subsequently was acquired by Avago technologies. At CyOptics/Avago, he continued work on EML development while additionally focusing on design, characterization, calibration, and qualification of liquid crystal external cavity tunable lasers for coherent applications. In 2014, he joined Freedom Photonics LLC, Santa Barbara, CA, USA, as the Director of Engineering. He is the author or co-author of more than 30 peer-reviewed journal papers.

Milan L. Mashanovitch (M'99–SM'13) received the Dipl.Ing. degree in electrical engineering from the University of Belgrade, Belgrade, Serbia, in 1998, and the Ph.D. degree in electrical engineering from the University of California, Santa Barbara, CA, USA, in 2004. He co-founded Freedom Photonics LLC, Santa Barbara, CA, USA, in 2005, and he has been in many technical roles related to product development and program management since. In addition to Freedom Photonics, he has worked for the University of California Santa Barbara, both as a Researcher on photonic integrated circuits, and as an Adjunct Professor teaching graduate level classes on semiconductor lasers and photonic ICs. He has co-authored nearly 130 papers, many invited, on photonic integrated circuits and various photonic devices. He is one of the authors of the second edition of the *Diode Lasers and Photonic Integrated Circuits* (Wiley, 2012). He has chaired, serves or has served on technical committees for IEEE Avionics, Fiber Optics and Photonics Conference, IEEE Microwave Photonics Conference, OSA's Integrated Photonics Research Conference, International Semiconductor Laser Conference, and Indium Phosphide and Related Materials Conference.

Leif A. Johansson (M'04) received the Ph.D. degree in engineering from the University College London, London, U.K., in 2002. He has been a Research Scientist with the University of California at Santa Barbara, Santa Barbara, CA, USA, and is the Founder of Freedom Photonics, Santa Barbara, CA, USA. His current research interests include design and characterization of integrated photonic devices for analog and digital applications and analog photonic systems and subsystems.

Larry A. Coldren (S'67–M'72–SM'77–F'82–LF'11) received the Ph.D. degree in electrical engineering from Stanford University, Stanford, CA, USA, in 1972. After 13 years in the research area with Bell Laboratories, he joined the University of California at Santa Barbara (UCSB), Santa Barbara, CA, USA, in 1984. From 2009 to 2011, he served as the the Dean of the College of Engineering. In 1990, he co-founded Optical Concepts, later acquired as Gore Photonics, to develop novel VCSEL technology, and, in 1998, he co-founded Agility Communications, later acquired by JDSU, to develop widely tunable integrated transmitters. At UCSB, he has worked on multiple-section widely tunable lasers and efficient vertical-cavity surface-emitting lasers (VCSELs). More recently, his group has developed high-performance InP-based photonic integrated circuits and high-speed VCSELs. He is currently the Fred Kavli Professor of Optoelectronics and Sensors and holds appointments in the Department of Materials and the Department of Electrical and Computer Engineering, UCSB. He has authored or coauthored more than a thousand journal and conference papers, co-authored eight book chapters, a widely used textbook, and holds 65 patents. He is a Fellow of OSA and IEE, and a member of the National Academy of Engineering. He received the 2004 John Tyndall Award, the 2009 Aron Kressel Award, the 2014 David Sarnoff Award, and the 2015 IPRM Award.